

Journal of Materials Chemistry A

Accepted Manuscript



This is an *Accepted Manuscript*, which has been through the Royal Society of Chemistry peer review process and has been accepted for publication.

Accepted Manuscripts are published online shortly after acceptance, before technical editing, formatting and proof reading. Using this free service, authors can make their results available to the community, in citable form, before we publish the edited article. We will replace this *Accepted Manuscript* with the edited and formatted *Advance Article* as soon as it is available.

You can find more information about *Accepted Manuscripts* in the [Information for Authors](#).

Please note that technical editing may introduce minor changes to the text and/or graphics, which may alter content. The journal's standard [Terms & Conditions](#) and the [Ethical guidelines](#) still apply. In no event shall the Royal Society of Chemistry be held responsible for any errors or omissions in this *Accepted Manuscript* or any consequences arising from the use of any information it contains.

ARTICLE

Nanoconfinement of Mg₆Pd particles in porous carbon: size effects on structural and hydrogenation properties

M. Ponthieu,^{a,b} Y. S. Au,^c K. Provost,^a C. Zlotea,^a E. Leroy,^a J.F. Fernández,^b M. Latroche,^a P.E. de Jongh^c and F. Cuevas^a

Received ooth,
Accepted ooth

DOI: 10.1039/x0xx00000x

www.rsc.org/

Mg₆Pd nanoparticles as small as 4 nm have been synthesized inside the pores of porous carbon. They are formed by infiltration of Mg on previously formed Pd nanoparticles dispersed into carbon. Their crystalline structure, as evaluated by X-Ray Diffraction (XRD) and X-ray Absorption Spectroscopy (XAS), differs from bulk Mg₆Pd since their particle size is close to the large crystal cell (~ 2 nm) of this intermetallic compound. Indeed, as compared to bulk Mg₆Pd, the nanoparticles exhibit a simpler crystallographic arrangement and a higher atomic disorder. Both thermodynamic and kinetic H-sorption properties of Mg₆Pd nanoparticles differ from those of bulk Mg₆Pd. The H-kinetics of the Mg₆Pd nanoparticles are significantly faster than bulk and are stable for at least 10 sorption cycles. Thermodynamic destabilization of the hydrided state is also observed for Mg₆Pd nanoparticles. Changes in the hydrogenation properties are attributed to nanosizing as well as to the modified structure of the nanoparticles as compared to bulk Mg₆Pd.

Introduction

Hydrogen storage in Mg-rich materials deserves strong interest because of the many inherent advantages of Mg. Magnesium is abundant, low-cost, non-toxic and able to store large amounts of hydrogen with a gravimetric capacity of 7.6 wt.% H. However, for room temperature applications, Mg cannot be used in pure state as it suffers from sluggish kinetics and unfavourable thermodynamics. Indeed, a temperature of 553 K is required to desorb hydrogen from MgH₂ at atmospheric pressure, according to the formation enthalpy and entropy of this binary hydride (-74.5 kJ/molH₂ and -135 J/KmolH₂, respectively¹).

Several strategies can be implemented to improve hydrogen sorption properties of Mg. One possibility is to alloy Mg with transition metals that possess good catalytic properties for hydrogen dissociation/recombination. Moreover, in some cases, the thermodynamics of such compounds are favourably modified. For example, the Mg₂Ni intermetallic compound forms the ternary hydride Mg₂NiH₄ which is less stable than MgH₂ ($\Delta H = -64$ kJ/molH₂ and $\Delta S = -122$ J/KmolH₂²). However, its reduced storage capacity of 3.6 wt.% H remains a barrier for its utilisation. The Mg-Pd system exhibits the attractive feature of forming the highly Mg-rich intermetallic compound Mg₆Pd³. This compound has attracted wide interest for hydrogen storage over the last decades as it is the lightest and also the cheapest Mg-Pd intermetallic. It is classified as a

complex metallic alloy: it crystallizes in a large face centred cubic (*fcc*) structure ($a = 20.108$ Å) containing 340 atoms of Mg and 56 atoms of Pd⁴. Huot *et al.* have demonstrated that it can store up to 4.3 wt.% H when exposed to 4 MPa of hydrogen pressure at 573 K⁵. Upon hydrogenation, Mg₆Pd decomposes into MgH₂ and Mg-poorer Mg-Pd intermetallics^{6,7}. The reported H-kinetics of Mg₆Pd are rather slow. No data is available so far on the reversibility of this material upon extended cycling.

Another way to enhance the hydrogenation properties of Mg is by downsizing. Nanosized materials exhibit faster kinetics than bulk alloys thanks to the shorter diffusion path length of H atoms and higher surface area available for hydrogen chemisorption. Moreover, first principles studies have demonstrated that the thermodynamics of nanosized materials can be altered as a consequence of the excess free energy of surface atoms with respect to bulk atoms⁸⁻¹⁰. According to Wagemans *et al.*, if the size of MgH₂ crystallites is reduced to 0.9 nm, hydrogen desorption at atmospheric pressure can occur at temperature as low as 473 K⁹. Significant destabilization of MgH₂ was predicted for crystallite smaller than 1.3 nm⁹ while Bérubé *et al.* calculated a reduction by more than 30 % of the enthalpy value for Mg crystals smaller than 5 nm⁸.

Nanostructuring can be achieved either by top-down or bottom-up methods. The most popular top-down technique is ball milling. It allows decreasing the particle and crystallite size from microcrystalline coarse to nanostructured fine powder by

means of mechanical energy¹¹. Ball milling is a very efficient technique to obtain nanostructured bulk materials with improved kinetic properties through the generation of oxide-free surfaces and lattice defects. Nevertheless, ball milled materials usually face the problem of crystal growth with temperature and/or H-cycling. Indeed, large crystals are energetically more favourable due to their lower interfacial energy. Alternatively, nanoparticles can be stabilized by confinement into the pores of a light and inert matrix (e.g. activated carbon) by means of bottom-up synthesis methods^{12,13}. For example, nanoparticles of Ni have been successfully deposited inside a porous carbon by impregnation of a nickel nitrate solution followed by drying and NiO reduction¹⁴. Another possibility is to infiltrate the active material, which is convenient for Mg as it melts at relatively low temperature (922 K) and has a high vapour pressure. This infiltration method was efficiently applied by de Jongh *et al.* to obtain Mg particles from 2 to 5 nm confined into an activated carbon¹⁵. Both methods have been combined to obtain Mg-Ni¹⁴ or Mg₂Cu¹⁶ alloy nanoparticles. Therefore, this innovative synthesis method is likely to be extended to a wide range of Mg-based alloys.

The present study aims to stabilize Mg₆Pd nanoparticles inside the pores of an activated carbon and characterize their hydrogenation properties as compared to the equivalent bulk alloy. To this purpose, Pd precursor particles are deposited into a porous carbon support followed by Mg infiltration. The textural properties of the composite are determined by N₂-physisorption and the structural properties of the confined alloy are thoroughly investigated by means of X-ray diffraction (XRD) and X-ray absorption spectroscopy (XAS). Solid-gas reactions were investigated to determine the thermodynamics and kinetics of (de)hydrogenation. We here demonstrate thermodynamic destabilization of hydrogen stored in Mg₆Pd nanoparticles as compared to the bulk as well as improvement of H-kinetics due to nanosizing effects.

Experimental

The preparation of nanoconfined Mg-based alloys in porous carbon requires a two-step specific procedure that has been recently developed^{14,15}. Pd nanoparticles are first deposited by impregnation of high surface area graphite (HSAG500 from TIMCAL) with Pd-containing aqueous solution (H₂PdCl₄) followed by the reduction of [PdCl₄]²⁻ ions in Ar-H₂ flow (0.5 L/min) at 573 K to obtain Pd@C composites^{17,18}. The Pd content in the Pd@C composite is 8.6(3) wt.%, as determined by inductively coupled plasma optical emission spectroscopy (ICP-OES). The sample was then outgassed under vacuum (10⁻³ Pa) for several hours and protected from air contact for all further handling. The second step consists in infiltration of Mg into this composite to get Mg₆Pd@C intermetallic/carbon material. The amount of added Mg corresponded to the stoichiometry of the intermetallic (Mg:Pd ratio of 6:1).

In the glove box, MgH₂ (Alfa Aesar 98 %) was mixed with the Pd@C composite and loaded in a graphite crucible which was

then placed in a non-hermetic stainless steel holder and introduced into a quartz tube. The tube was then placed in a furnace under Ar flow and heated up to 923 K to decompose MgH₂ and to reach infiltration of the molten Mg into the carbon pores. After 40 minutes of dwelling, the sample was cooled down slowly and transferred to the glove box. The final metal loading in the Mg₆Pd@C composite is 18.5(5) wt.%. ICP-OES analysis of the intermetallic counterpart yields 63(1) wt.% Mg, which approaches the Mg-rich limit of the Mg₆Pd phase (61.3 wt.% Mg) determined by Makongo *et al.*¹⁹. Finally, the composite material was hydrogenated overnight in a high pressure autoclave (Parr) at 573 K under a hydrogen pressure of 5 MPa. The hydrogenated sample is labelled as Mg₆Pd@C-H.

The porosity and surface area of the pristine carbon and composite materials were determined by measuring adsorption and desorption nitrogen isotherms at 77 K using a Micromeritics instrument. The specific surface area was calculated by using the Brunauer, Emmett and Teller (BET) method²⁰ within the 0.05-0.25 relative pressure range. The total pore volume was deduced from the amount of adsorbed nitrogen close to the saturation pressure ($P/P_0 = 0.99$ in the isotherm).

Transmission electron microscopy (TEM) bright and dark field images were recorded to characterize the particles size and distribution inside the pores of the carbon. The air-sensitive samples were loaded inside the glove-box using a special air-protective sample holder (Gatan CHVT3007). The thin powder was dispersed on a 300 mesh Cu holey carbon grid. In addition, the sample holder was cooled to ~100 K with liquid nitrogen to avoid decomposition of the hydrided samples by beam irradiation. The microscope was a FEI Tecnai F20 ST with a field emission gun operated at 200 keV.

The structural characterization of the pristine carbon and the composite materials was performed initially by XRD using a Bruker D8 Advance θ - θ diffractometer equipped with Cu-K α radiation ($\lambda_{K\alpha 1} = 1.54051$ Å, $\lambda_{K\alpha 2} = 1.54433$ Å) and backscattered rear graphite monochromator. A special air-tight sample-holder commercialized by Bruker was used to prevent sample oxidation. Detailed information on the local structure of the alloyed nanoparticles was obtained by XAS experiments. Pellets of Mg₆Pd bulk reference mixed with boron nitride (30 mg in 20 mg), Mg₆Pd@C and Mg₆Pd@C-H composites (~160 mg) were prepared in the glove box, and kept under He atmosphere in a closed cell. XAS spectra of Mg₆Pd bulk and Mg₆Pd@C composite were recorded in transmission, at the Pd K-edge, at the DESY-synchrotron facility in Hamburg (DORIS beamline C). The quantities used in the pellets resulted in an edge jump of $\Delta\mu_x \sim 0.8$ -0.9. The spectra were extracted using standard procedures available in MAX-Cherokee program²¹ ($E_0 = 24356$ eV, Fourier transform range 2.8-11.45 Å⁻¹). All EXAFS fits were performed with MAX-RoundMidnight code²¹ by fitting the experimental spectra to the EXAFS standard formula, using first-coordination sphere filtered spectra. Theoretical phases and amplitudes were calculated with FEFF8.4 code^{22,23} on the basis of Mg₆Pd⁴ and MgPd²⁴ crystallographic structures. Statistical errors and error bars were

evaluated as recommended by the IXS Standard and Criteria Subcommittee²⁵. According to these recommendations, the goodness of fit was evaluated using the reduced $\Delta\chi^2$ minimum or quality factor (QF). The number of different Pd-Mg distances in the Mg-rich phases was evaluated, as proposed by Moscovici *et al.*²⁶, by following the QF evolution when the number of independent distances increases.

Isothermal absorption curves were measured by solid-gas reaction in a home-made Sievert's manometric apparatus at 573 K. A typical mass of 200 mg of bulk and nanoconfined materials were cycled between $P_{\text{abs}} = 4.5$ MPa and $P_{\text{des}} = 0.03$ MPa. Pressure-composition isotherms (PCI) were also measured at 548 K between 0.01 and 1 MPa. Thermal desorption spectroscopy (TDS) experiments were carried out under secondary vacuum ($P_{\text{res}} = 2.10^{-4}$ Pa) by heating up to 823 K at 5 K/min about 10 mg of hydrided sample. The amount of desorbed hydrogen was measured with a quadrupole mass spectrometer MKS Microvision Plus RGA. Finally, bulk and nanoconfined samples have been thermally cycled by high pressure differential scanning calorimetry (HP-DSC) under a hydrogen pressure of 0.5 MPa. Samples with typical mass of ~10 mg were loaded in a high pressure cell and introduced into the furnace of the SENSYS evo DSC instrument from Setaram.

Results and discussion

Textural properties of the composite materials.

The N_2 -physorption isotherms (Figure 1) have been measured for the composite materials after each step of the synthesis. All values are reported per gram of carbon. The main results extracted from BET calculations are shown in Table 1. After Pd impregnation, a minor decrease of surface area from 500 to 460 m^2/g is observed and the total pore volume of pristine carbon decreases from 0.69 to 0.61 cm^3/g . This decrease exceeds the volume that corresponds to the deposited Pd amount (0.01 cm^3/g) and indicates partial obstruction of the carbon micropores by the Pd nanoparticles. After Mg infiltration, the total pore volume decreases to 0.51 cm^3/g and the surface area is strongly reduced to 320 m^2/g . Such a large decrease of the BET surface area is attributed to pore blocking effects. Mg infiltrates the same pores as those containing the Pd nanoparticles, making possible the reaction of both elements within the pores to form intermetallic nanoparticles.

Table 1. BET surface area and total pore volume of pristine carbon (HSAG500) and composite materials. All values are given per gram of carbon.

Sample	S (BET) (m^2/g)	Total pore volume (cm^3/g)	Expected volume loss (cm^3/g)
HSAG500	500(10)	0.69(1)	-
Pd@C	460(10)	0.61(1)	0.01
Mg ₆ Pd@C	320(7)	0.51(1)	0.07
Mg ₆ Pd@C-H	262(6)	0.41(1)	-

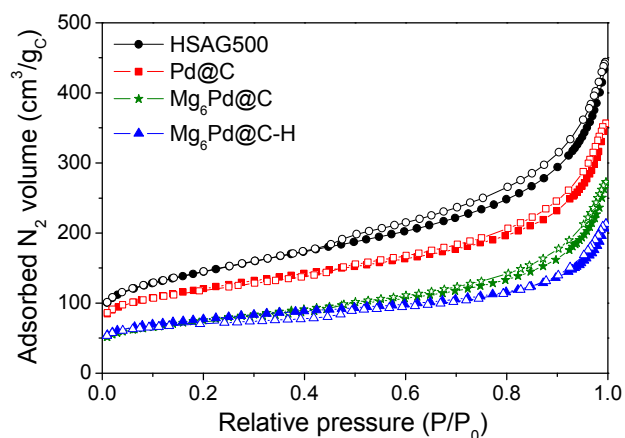


Figure 1. Nitrogen physisorption isotherms of pristine HSAG500 after Pd impregnation (Pd@C), after infiltration of Mg (Mg₆Pd@C) and after hydrogenation (Mg₆Pd@C-H). Full symbols correspond to the adsorption and empty symbols to the desorption branches.

Upon hydrogenation, the BET surface area slightly decreases to 262 m^2/g and the total pore volume is reduced to 0.41 cm^3/g . Both the volume expansion of the active material upon hydrogen absorption as well as pore obstruction may contribute to this decrease.

Micro-structural properties of the composite materials.

TEM was performed on the composite samples to determine the size and distribution of the nanoparticles in the carbon matrix (Figure 2).

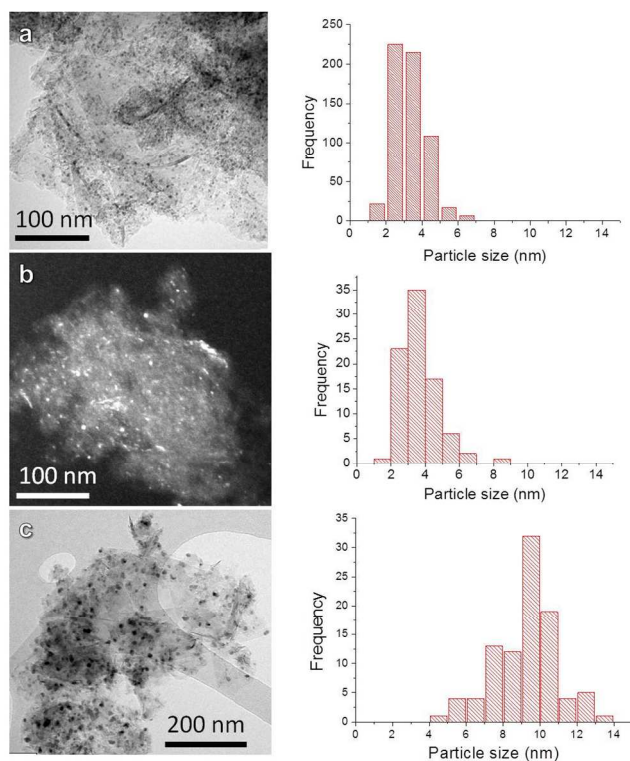


Figure 2. TEM images of a) Pd@C, b) Mg₆Pd@C and c) Mg₆Pd@C-H samples. The histograms on the right display the size distribution of the nanoparticles.

The Pd@C composite exhibits a homogeneous distribution of Pd nanoparticles with an average particle size of 3 nm. After Mg infiltration, the mean particle size slightly increases to 4 nm and the homogeneous distribution is maintained. After hydrogenation, the particle size clearly increases to ~ 10 nm which implies long-range diffusion of metal species.

Structural properties of the composite materials

XRD ANALYSIS Figure 3 shows the XRD patterns of the four studied materials. For the Pd@C composite, besides diffraction lines from carbon, diffraction peaks from *fcc* Pd at $2\theta = 40, 47$ and 68° (corresponding to (111), (200) and (220) planes, respectively) are observed. For the Mg₆Pd@C composite, beside the carbon signals, two broad peaks corresponding to the strongest lines of the Mg₆Pd compound are observed. They are located at $2\theta = 21.5^\circ$ and 38.0° , respectively, which matches the (422) and (822) reflections of the Mg₆Pd crystal structure⁴. The fact that neither pure Mg nor Pd phases were detected confirms that Mg reacted with the Pd nanoparticles during the infiltration process. However, the quality of the XRD data of the Mg₆Pd@C composite is not sufficient to ensure the formation of Mg₆Pd phase as several Mg-Pd intermetallic phases, such as Mg₅Pd₂, possess their main diffraction peaks at similar diffraction angles. The occurrence of broad diffraction peaks for Pd@C and Mg₆Pd@C composites concurs with the formation of nanocrystalline particles within the pores of the carbon host, in agreement with the textural analysis (Figure 1) and the TEM observations (Figure 2a and b).

Regarding the hydrided material, the formation of the MgH₂ phase (rutile-type structure) and the MgPd intermetallic (CsCl-type structure) is clearly identified. The MgPd intermetallic compound exhibits much broader peaks than the MgH₂ phase, revealing a smaller coherent diffraction length for the former phase. Minor MgO contamination was also detected as result of partial reaction with air traces during sample handling.

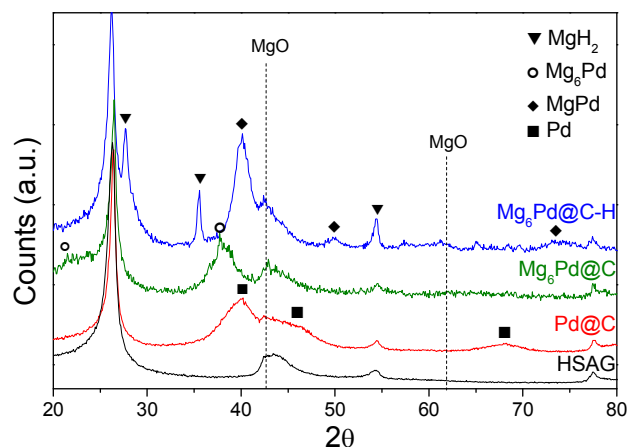


Figure 3. XRD patterns (Cu-K α radiation) and phase identification of pristine HSAG, Pd@C, Mg₆Pd@C and Mg₆Pd@C-H composites.

XAS ANALYSIS. To gain a deeper insight in the structural properties of the Mg-Pd phases formed during infiltration with Mg and after hydrogenation, XAS measurements at the Pd K-edge have been performed. The as-synthesized Mg₆Pd@C composite was measured and compared to a bulk Mg₆Pd reference as well as a Pd foil standard. Figure 4 displays the experimental EXAFS spectra and corresponding Fourier Transforms (FT). The Mg₆Pd-based samples exhibit a smaller EXAFS amplitude than the Pd foil and a clear phase shift. This fact reveals the presence of Mg atoms around Pd atoms and therefore the occurrence of a Mg-Pd phase for both bulk and nanoconfined Mg₆Pd samples. The weakest signal is obtained for the bulk Mg₆Pd, as clearly observed on the first peak of the FT (Figure 4b). This low signal is explained by interference effects related to the complex crystallographic structure of this phase. Indeed, the Mg₆Pd crystal includes 4 independent Pd sites, resulting in 14 different Pd-Mg distances (see Figure S1 in supplementary information).

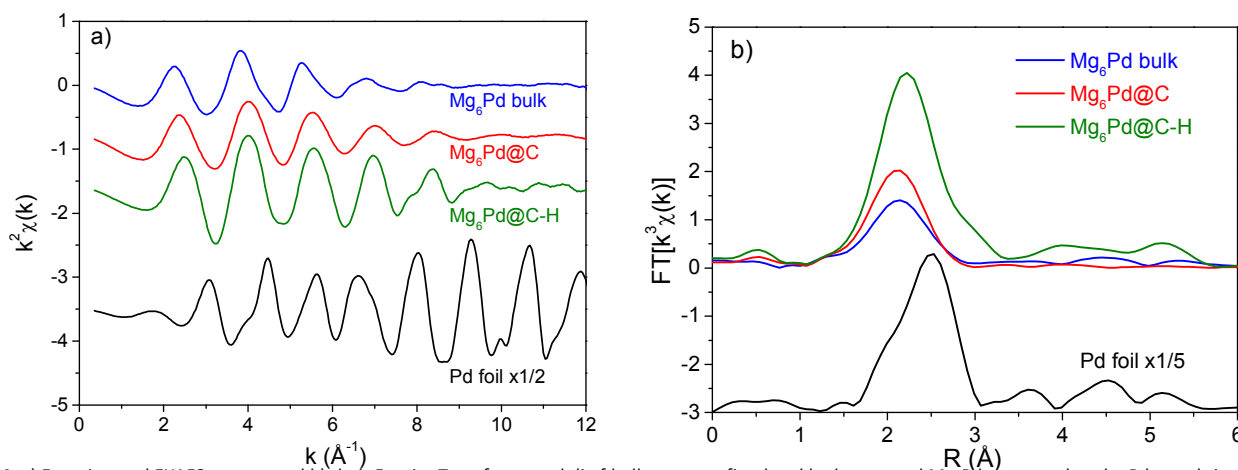


Figure 4. a) Experimental EXAFS spectra and b) their Fourier Transform moduli of bulk, nanoconfined and hydrogenated Mg₆Pd compared to the Pd metal signal.

Table 2. Refined structural parameters of EXAFS spectra for the first coordination sphere around the Pd atom using a two-paths (Pd-Mg and Pd-Pd) model. N_i is the number of i atoms situated at a distance R_i of a Pd centre. σ^2 is the Debye-Waller factor and QF_k and QF_R are the quality factors in k - and R -spaces, respectively. Comparison with XRD data is provided.

		N_{Mg}	R_{Mg} (Å)	N_{Pd}	R_{Pd} (Å)	σ^2 (Å ²)	QF_k	QF_R
Short range order (EXAFS)	Pd foil	0(1)	–	11(1)	2.74(1)	0.006(1)	1.64	2.24
	Mg ₆ Pd	11(2)	2.84(2)	0(2)	–	0.033(5)	1.61	1.88
	Mg ₆ Pd@C	7(2)	2.75(2)	0(3)	–	0.021(6)	2.59	2.36
	Mg ₆ Pd@C-H	8(2)	2.74(1)	2(1)	3.14(5)	0.012(3)	3.85	2.57
Long range order (XRD)	Pd metal ²⁴	0	–	12	2.75			
	Mg ₆ Pd ⁴	10.86	2.89(23)	0	–			
	MgPd ²²	8	2.75	6	3.17			

The corresponding signals imply the occurrence of destructive interferences that reduce the signal intensity of the FT main peak (Figure S2 in supplementary information). In contrast, the Mg₆Pd@C composite presents a larger FT first peak, but almost no signal at longer distances, which is a typical signature of highly disordered materials. Upon hydrogenation, the intensity of the FT first peak increases and a non-negligible signal appears between 3 and 6 Å. For all samples, the Fourier-filtered EXAFS spectra were initially fitted using a two-paths model with Pd atom surrounded by Mg and/or Pd atoms at single distances in the first coordination sphere. The results are displayed in Table 2. As expected from long-range crystallographic structures (*i.e.* XRD data), only Pd was detected in the Pd foil, whereas the fitted number of Pd atoms converged to zero in bulk Mg₆Pd. Interestingly, a similar result was found for nanoconfined Mg₆Pd. In both cases, the neighbouring atoms within the first sphere around a Pd atom only consist of Mg, confirming the presence of a Mg-rich phase.

Next, the structures of the Mg₆Pd bulk reference and Mg₆Pd@C composite have been refined more accurately by using several fitting models with increasing complexity. In fact, full refinement of the 14 interatomic Pd-Mg distances in Mg₆Pd is not feasible. Therefore, to minimize the number of fitting parameters, the number of distances was simplified, starting from 1 up to 4 average Pd-Mg distances (R_i), while maintaining a total coordination number (CN) close to 11 (see Table S1 in supplementary information). The graphical outputs of the EXAFS fits using a 1, 2 or 3-distances model for bulk and nanoconfined Mg₆Pd are illustrated in Figure 5.

For the bulk material, there is a continuous improvement of the fit quality from one to three independent Pd-Mg distances (Figure 5a and b). In the 3-distances model, the slight difference on the left of the FT peak suggests that using a 4-distances model by splitting the shorter distance R_1 (which contains 5.7 Mg at 2.79(10)Å) into two distances (1.7 Mg at 2.69(3)Å and 4.0 Mg at 2.84(5)Å) would probably improve the fit. However, due to correlations, it was not possible to free all parameters for 4 independent distances. This result shows that at least three different distances are necessary to describe the average environment of Pd atoms in bulk Mg₆Pd. The best

results, corresponding to the 3-distances model, are gathered in Table 3. The refined distances are in good agreement with the average crystallographic ones derived from XRD data.

In the case of the nanoconfined particles, the 2-distances model already gives a good description of the FT peak shape, and no fit improvement is observed when introducing a third independent distance (Figure 5c and d). This result indicates the less complex atomic arrangement in nanoparticles than in bulk Mg₆Pd, which concurs with the more intense FT signal of the former (Figure 4b). However, the larger Debye-Waller factor observed for the nanoparticles indicates a larger atomic disorder than for the bulk alloy. EXAFS refinements also reveal that the weighted average Pd-Mg distance is ~0.1 Å shorter for the nanoparticles ($R = 2.80$ Å) than for the bulk material ($R = 2.92$ Å). Such a reduction of the first neighbour distances in nanoparticles was also observed in other systems^{27,28}, especially when the ratio between particle size and cell parameter is lower than 2.6²⁸. For Mg₆Pd@C, this ratio is particularly low (~2) as result of the small particle size (~4 nm) and the large cell parameter ($a = 20.108$ Å) of the confined nanoparticles. To summarize, the crystal structure of Mg₆Pd nanoparticles is slightly different from that of the bulk phase. The atomic ordering is simpler (*i.e.* lower number of different Pd-Mg distances) but more disordered (*i.e.* higher Debye-Waller factor). These differences likely arise from the approaching of the characteristic length of nanoparticles to the Mg₆Pd lattice parameter.

For the hydrogenated Mg₆Pd@C-H composite, Pd atoms are detected in the Pd first coordination sphere (Table 2). Pd-Mg and Pd-Pd distances are in good agreement with MgPd XRD distances. Using a single Debye-Waller factor, the number of Mg atoms in the Pd first environment is in good agreement with MgPd crystal structure but the number of Pd atoms is lower than expected. If the numbers of Pd and Mg atoms are constrained to their crystallographic values, the Debye-Waller factor of Pd becomes twice larger than that of Mg, which is surprising if it would be assigned to thermal vibrations. Interestingly, a similar difference in the Pd-Mg and Pd-Pd Debye-Waller factors was observed by Pasquini *et al.* in MgPd nanoparticles of similar sizes (10 nm for Mg₆Pd@C-H, 12 nm for MgPd nanoparticles in Pasquini's paper²⁹). This difference

was reasonably attributed to the occurrence of Mg_3Pd and Mg_5Pd_2 phases in the hydrogenated nanoparticles. Furthermore, as shown in Figure 6, we observe that the signal beyond the FT first peak is in good agreement with the signal expected for a MgPd phase. No distance contraction is observed, which may

be related to the larger particle size and lower cell parameter of MgPd as compared to Mg_6Pd nanoparticles. Moreover, the lower Debye-Waller factor indicates less disordered nanoparticles after hydrogenation.

Table 3. Mg atoms distribution within the first coordination sphere of a Pd atom as calculated from XRD data and as fitted for Mg_6Pd bulk and nanoparticles for the 3-distances model. N_i is the number of Mg atoms situated at a distance R_i of a Pd centre. σ^2 is the Debye-Waller factor and QF_k and QF_R are the quality factors in k - and R -spaces, respectively.

	N_1	R_1 (Å)	N_2	R_2 (Å)	N_3	R_3 (Å)	σ^2 (Å ²)	QF_k	QF_R
Crystallographic average distances	5.7	2.79(10)	3.4	2.96(3)	1.7	3.12(1)	-	-	-
Mg_6Pd bulk	4(3)	2.76(8)	5(1)	2.95(11)	2	3.18(17)	0.012(9)	0.61	0.3
$\text{Mg}_6\text{Pd}@C$	8(7)	2.73(2)	3	3.00(5)	-	-	0.017(3)	0.8	0.68

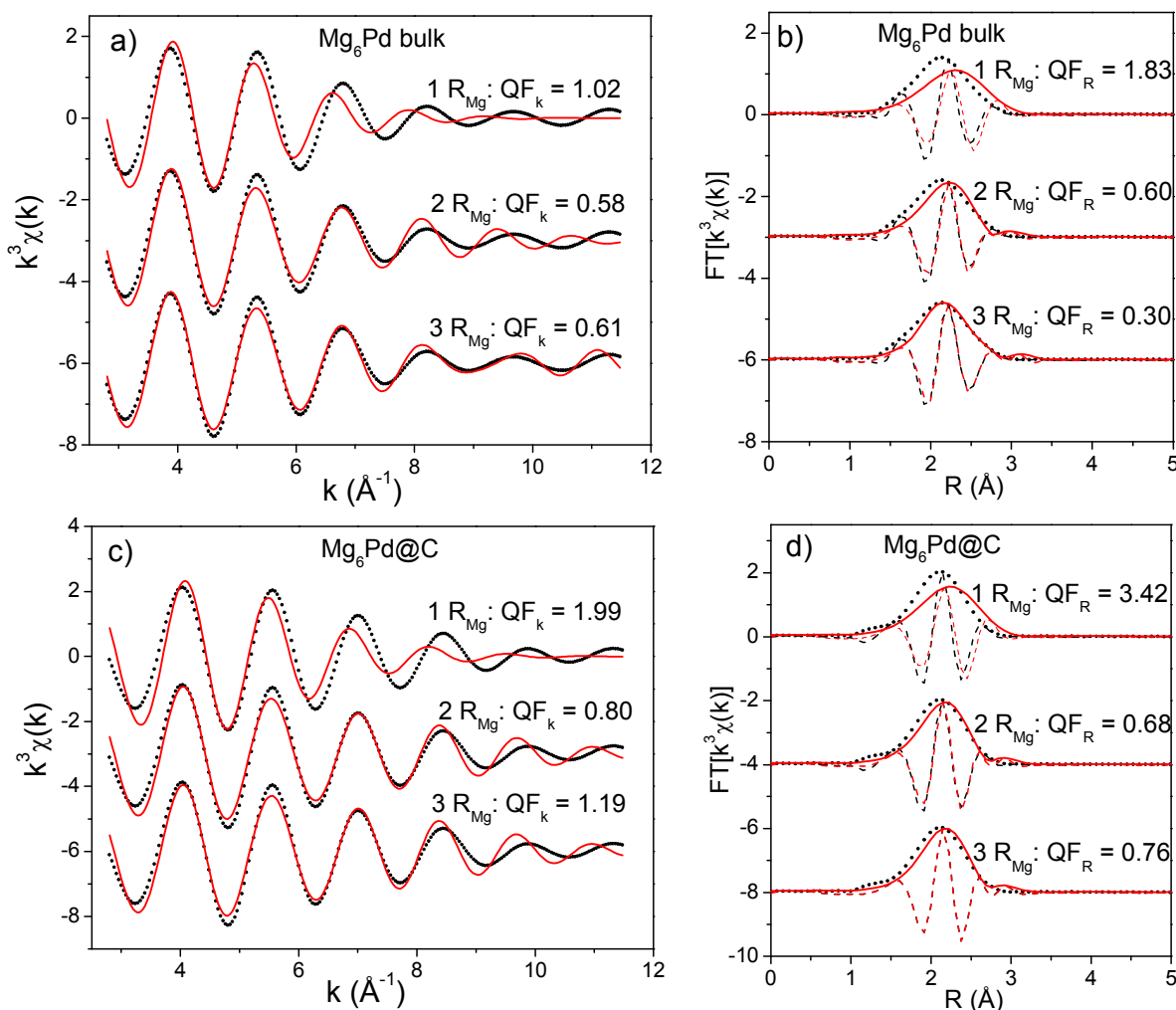


Figure 5. EXAFS (left) and FT (right) spectra fitted using the 1-, 2- and 3-distances models applied to (a, b) bulk Mg_6Pd and (c, d) $\text{Mg}_6\text{Pd}@C$. Black symbols represent the experimental signal and red lines the theoretical signal. Continuous and dashed lines correspond to modulus and imaginary part, respectively.

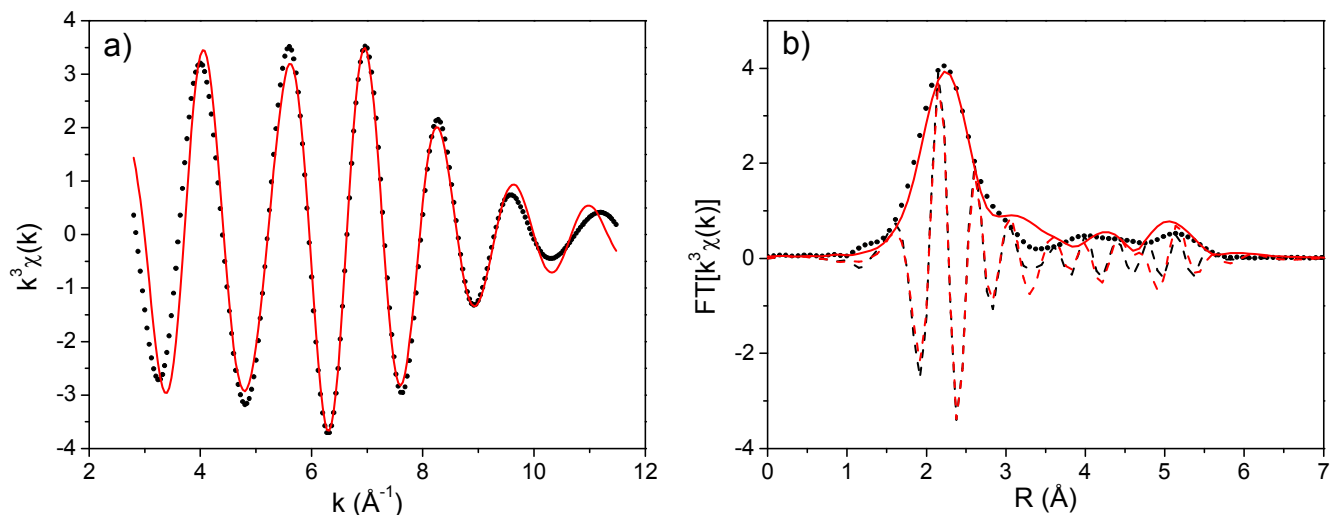


Figure 6. a) EXAFS and b) FT spectra of hydrogenated $\text{Mg}_6\text{Pd}@C\text{-H}$ composite sample. Black symbols represent the experimental signal and red lines the theoretical signal obtained from the Mg_6Pd structure. Continuous and dashed lines correspond to modulus and imaginary part, respectively.

Hydrogenation properties of the Mg_6Pd nanoparticles compared to Mg_6Pd bulk

THERMODYNAMIC PROPERTIES Equilibrium hydrogen sorption properties for nanoconfined and bulk Mg_6Pd were compared based on PCI measurements (Figure 7). The isotherms for the bulk alloy display a flat plateau though, as reported by Yamada *et al.*⁷ and Huot *et al.*⁵ two (de)hydrogenation reactions leading to the successive formation of $\text{Mg}_{3.65}\text{Pd}$ and Mg_5Pd_2 may occur in the studied pressure range. In contrast, the nanostructured compound exhibits a sloping plateau at much higher equilibrium pressure. This result highlights either the destabilization of the hydrided state or the stabilization of the metallic nanoparticles, which both result in a reduced enthalpy of reaction, due to nanosizing. In addition, the local disorder of the nanoparticles revealed by XAS analysis may account for the sloping nature of the plateau. Indeed, hydrogen absorption in disordered alloys is characterised by a broad distribution of hydrogen binding energies^{30,31}. One can also notice that, as result of the nanoconfinement effect, the hydrogen uptake is lower for nanocrystalline (1.7 wt.%) than for bulk (2.5 wt.%) Mg_6Pd at the maximum attained pressure of 1 MPa.

The thermodynamic improvement of the $\text{Mg}_6\text{Pd}\text{-H}$ system by nanosizing has also been evidenced through HP-DSC analysis. Figure 8 shows hydrogen desorption/absorption cycles for both nanoconfined and bulk Mg_6Pd under $P_{\text{H}_2} = 0.5$ MPa. Exothermic and endothermic peaks correspond to hydrogen absorption and desorption, respectively. For the $\text{Mg}_6\text{Pd}@C$ compound, the onsets of both reaction peaks are shifted to lower temperatures. If one assumes that the equilibrium temperature is midway between the reaction onsets (*i.e.* energetically equivalent kinetic barriers operate for absorption and desorption³²), its value is 18 K lower for the nanoconfined than for the bulk compound (see Figure 8). This result indicates the smaller enthalpy variation for the hydrogenation of the

nanoconfined compound as compared to the bulk one. Indeed, according to the Van't Hoff relationship ($\ln \frac{P_p}{P_0} = \frac{\Delta H}{RT} - \frac{\Delta S}{R}$), for a metal-hydrogen system working under isobaric conditions, the less stable one (*i.e.* with smallest ΔH) exhibits the lowest plateau temperature. It is also worth noting in HP-DSC runs that sharper calorimetric peaks occur for the composite material as compared to the bulk sample. This reflects faster sorption kinetics for the nanometric particles in agreement with kinetic measurements described below.

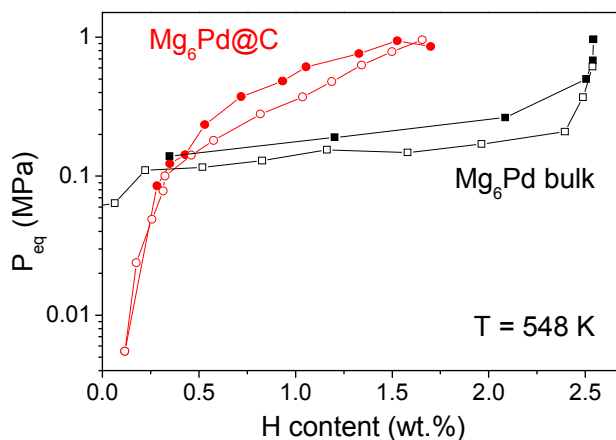


Figure 7. Hydrogen sorption isotherms at 548 K for the bulk (black line) and nanoconfined (red line) Mg_6Pd . Full and empty symbols stand for absorption and desorption isotherm curves, respectively.

Though previous results do not allow a precise evaluation of the thermodynamic destabilization in the $\text{Mg}_6\text{Pd}\text{-H}$ system, clear evidences of the thermodynamic modification due to size effects are given. This destabilization can be attributed to two main phenomena:

- i) The non-negligible free surface energy related to the nanosized particles results in a less stable hydride with

respect to the metal phase if the surface energy of the hydride is larger than that of the metal. This effect has already been anticipated by *ab initio* calculations⁹, though contradictory calculations have recently been reported³³ and up to now very few experimental results support this assumption. An enthalpy of absorption of -63.8 kJ/molH₂ was reported for MgH₂ nanoparticles smaller than 3 nm³⁴ as compared to -74.5 kJ/molH₂ for bulk MgH₂. However, this enthalpy reduction was accompanied by a less negative entropy value and the effective change on the desorption temperature was limited to 11 K at 0.1 MPa of hydrogen pressure. In our case, the effective destabilization seems to be more significant: 18 K as estimated from HP-DSC measurements. It is likely that the occurrence of nanoscale Mg-Pd intermetallics that accompany MgH₂ formation account for such a higher destabilization.

- ii) The structure of nanoscale Mg₆Pd is significantly modified as compared to the bulk as observed by XAS. As a matter of fact, the size of the nanoparticles (4 nm) is very close to that of the crystallographic cell of the bulk ($a \sim 2$ nm) and therefore the long range order structure cannot be retained for such small particles. Thus, the structural disorder may alter the H-stability as compared to bulk. However, such effect might be also considered as an indirect consequence of the size reduction.

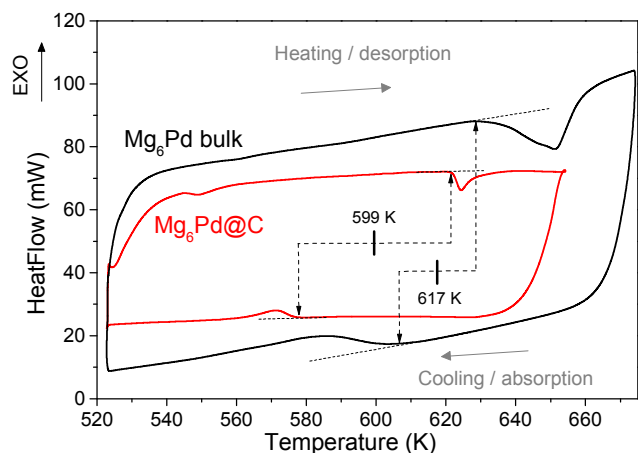


Figure 8. HP-DSC measurements obtained during heating and cooling ramps (heating rate = 5 K/min) under 0.5 MPa of hydrogen isobaric pressure on bulk (black line) and nanoconfined (red line) Mg₆Pd. Equilibrium temperatures for hydrogen sorption for both samples are estimated as mid-values between the corresponding peak onsets.

KINETIC PROPERTIES AND CYCLABILITY *Isothermal hydrogen absorption:* Kinetics of absorption have been tested in a Sievert's apparatus over 10 sorption cycles for both nanoconfined Mg₆Pd and its bulk counterpart. The absorption curves of cycles 2, 5 and 10 are displayed in Figure 9. The first H-absorption was sluggish for the bulk sample due to activation concerns and is not represented. For the composite material, this step was not necessary; the first absorption was similar to the second one. The absorption kinetics in the nanoconfined material is about five times faster than in the bulk sample

during the second absorption. This fast kinetics is attributed to the nanometric particle size which provides higher active surface for H-chemisorption and shorter H-diffusion path. In addition, we observe a rapid decay of the H-kinetics for the bulk material after few cycles (Figure 9). The tenth absorption deterioration can be explained by the decomposition of Mg₆Pd into MgH₂ and Mg-poor Mg-Pd intermetallics upon hydrogenation with phase separation over long distances. Thus, the alloy recombination step is not fully completed on MgH₂ desorption due to the slow diffusion kinetics of metallic atoms at 573 K. In contrast, the nanoconfined Mg₆Pd exhibits steady absorption rates, even after 10 cycles. This result suggests that the nanometric size of the active material is maintained to a certain extent, by means of the physical barrier provided by the carbon pores to avoid coalescence. In consequence, the diffusion length of the metallic atoms remains very short and allows for fast alloy recombination and short H-diffusion length.

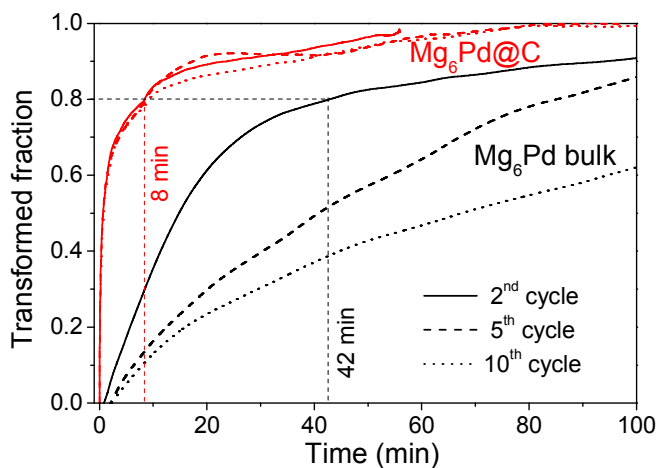


Figure 9. Time-evolution of the transformed fraction during isothermal H-absorption in cycles 2, 5 and 10 for bulk and nanoconfined Mg₆Pd. $T = 573$ K, $P_{\text{abs}} = 4.5$ MPa.

Figure 10 shows the XRD pattern of the desorbed Mg₆Pd@C after 10 cycles of absorption and desorption at 573 K. Besides diffraction peaks from the Mg₆Pd phase, the three characteristic peaks of the *hcp* Mg phase at $2\theta = 32.2$, 34.4 and 36.6° corresponding to (100), (002) and (101) reflections are observed. Mg-peaks are relatively sharp. Again, MgO contamination could not be fully avoided. In addition, a broad peak is observed around 40° and a shoulder appears on both sides of the main carbon peak. According to mass balance considerations, these peaks must belong to a Mg-Pd phase with Mg-content lower than initial Mg₆Pd. For instance, the Mg₂Pd phase (with main diffraction peaks at $2\theta = 25.6$ and 38.8° ³⁵) and the η -Mg₃Pd phase (at $2\theta = 24.7$ and 39.0° ³⁶) are good candidates. Unfortunately, the width and overlapping of the diffraction peaks do not allow us to give a conclusive peak assignment. Anyway, this result indicates that a certain irreversibility occurs in the composite system as result of Mg

segregation. However, the persistence of broad diffraction peaks leads to believe that the nanoconfinement was preserved and thereby fast hydriding kinetics.

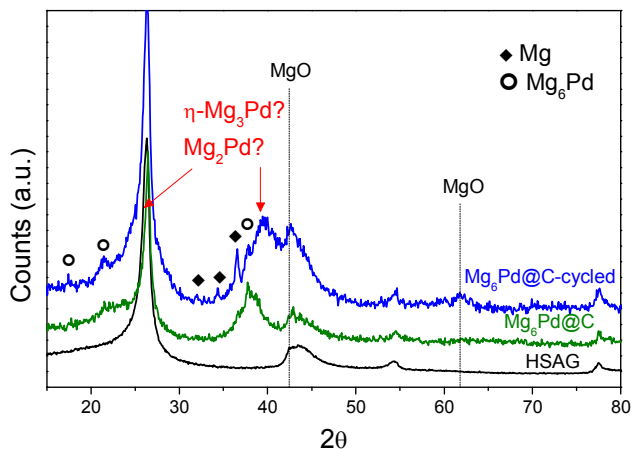


Figure 10. XRD patterns (Cu K_{α} radiation) and phase identification of Mg_6Pd/C before and after 10 H-sorption cycles at 573 K. The pattern for the pristine carbon (HSAG) is displayed at the bottom.

Dufour *et al.*⁶ have shown that hydrogenation of bulk Mg_6Pd induces the formation of MgH_2 together with a Mg-Pd intermetallic phase which composition depends on the pressure and temperature conditions. Therefore, H-absorption is accompanied by the diffusion of Mg and Pd atoms over long distances. In the case of the nanoconfined Mg_6Pd , a similar mechanism occurs: the formation of MgH_2 and $MgPd$ is clearly detected by XRD (Figure 3). Moreover, TEM images (Figure 2) show that hydrogenation causes an increase of the particle size. Considering the occurrence of Mg phase on desorption (Figure 10) and the relatively sharp peaks of MgH_2 in the absorbed state (Figure 3), we can infer that Mg tends to coalesce and to migrate into large pores on cycling. In contrast, Mg-Pd intermetallics seem to remain at nanometric scale (as revealed by the broad diffraction peaks in Figures 3 and 10) into the smallest pores. This process is responsible for the limited reversibility of the composite, making difficult to fully recover the original intermetallic Mg_6Pd .

Thermal desorption. The H-desorption properties have also been analysed by means of TDS (Figure 11). For the bulk sample, the desorption begins around 650 K with a single and rather sharp peak. The $Mg_6Pd/C-H$ composite starts to desorb at much lower temperature with a first broad peak between 370 and 515 K, followed by a more intense peak around 600 K. For both samples, the main peak at high temperature is attributed to H-desorption from the MgH_2 phase. However, desorption from the nanoparticles occurs 100 K lower than from the bulk powder. This is attributed to the shortening of H-diffusion path for the composite material, as shown previously for pure MgH_2 nanoparticles confined into carbon¹³. In addition, the broadening of the desorption peak as compared to bulk Mg_6Pd results of the size distribution of the hydride nanoparticles. The contribution of carbon to the accelerated desorption process has also to be considered, as it has already been reported to

facilitate H-release^{16,37}. However, this effect was recognized of minor importance in comparison with the nanosizing effect. Regarding the low temperature peak observed during H-desorption from the composite material, it can be tentatively attributed to hydrogen interactions with surface hydroxides³⁸, the relative amount of which is significant due to the high specific surface area of the nanoparticles and oxygen impurities in glove box.

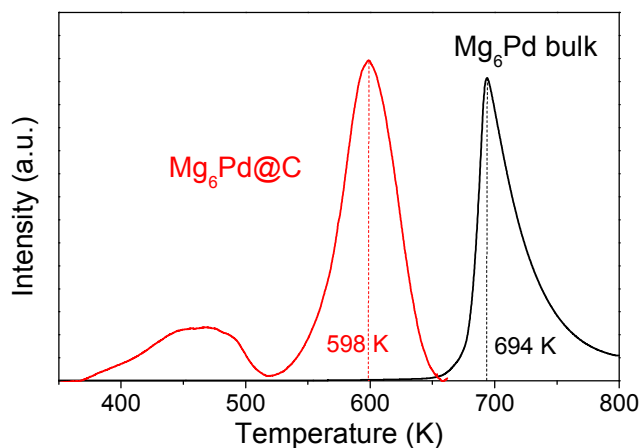


Figure 11. Thermal desorption hydrogen spectra at 5 K/min of hydrogenated bulk (black line) and nanoconfined (red line) Mg_6Pd .

Conclusions

We have demonstrated that it is possible to impregnate a porous carbon matrix with Pd and Mg successively and by *in situ* reaction form intermetallic Mg_6Pd nanoparticles. The structural characterisation of Mg_6Pd nanoparticles by XRD is difficult because of the low crystallinity of the alloy and the complexity of the Mg_6Pd structure. This problem is circumvented by EXAFS analysis that demonstrates the formation of Mg_6Pd nanoparticles with simpler atomic ordering as compared to the bulk counterpart.

The particle size is about 4 nm in the as-synthesized compound and increased to 10 nm after hydrogenation. PCI and HP-DSC experiments demonstrate thermodynamic destabilization of Mg_6Pd-H system in nanoparticles, confirming the various *ab initio* predictions and the importance of particle size. During reversible isothermal hydrogen absorption, the nanoparticles exhibit significantly faster reaction rate than the Mg_6Pd bulk material. The confinement of the active material into the pores is efficient to preserve this fast kinetics during at least 10 cycles. Indeed, the coalescence of the particles is limited, even though minor Mg segregation could not be avoided. The enhanced kinetic and cycling properties of the Mg_6Pd/C compound are explained by the reduced H-diffusion path and the high specific surface area available for hydrogen dissociation and nucleation of the MgH_2 phase. This work demonstrates that nanoconfinement can be of strong interest to develop Mg-based storage materials with improved hydrogenation properties for practical applications.

Acknowledgements

The authors wish to thank Diana Dragoë and Junxian Zhang for ICP-OES analyses, TIMCAL for providing the high surface area graphite and the DORIS-beamline of DESY-synchrotron for EXAFS measurements. We also acknowledge the MP1103 COST Action “Nanostructured materials for solid-state hydrogen storage”, the French-Dutch PHC-NWO Van Gogh program and the Spanish Ministry of Education and Science (contract number MAT 2011-22780) for financial support.

Notes and references

^a ICMPE/CNRS-UPEC UMR 7182, 2-8 rue Henri Dunant, 94320 Thiais, France.

^b Dpto. Física de Materiales, Facultad de Ciencias, Universidad Autónoma de Madrid, 28049, Madrid, Spain.

^c Inorganic Chemistry and Catalysis, Debye Institute for Nanomaterials Science, Utrecht University, Universiteitsweg 99, 3584 CG Utrecht, The Netherlands.

Electronic Supplementary Information (ESI) available: Detailed information on the atomic distribution around Pd sites and their average values for 3R- and 4R-models. Theoretical EXAFS spectra and FT moduli for each Pd site and resulting average signal.

- J. F. Stampfer, C. E. Holley, and J. F. Suttle, *J. Am. Chem. Soc.*, 1960, **82**, 3504–3508.
- J. Reilly and R. Wiswall, *Inorg. Chem.*, 1968, **7**, 2254–2256.
- H. Okamoto, *J. Phase Equilibria Diffus.*, 2010, **31**, 407–408.
- S. Samson, *Acta Crystallogr.*, 1972, **B28**, 936.
- J. Huot, A. Yonkeu, and J. Dufour, *J. Alloys Compd.*, 2008, **475**, 168–172.
- J. Dufour and J. Huot, *J. Alloys Compd.*, 2007, **446–447**, 147–151.
- T. Yamada, J. T. Yin, and A. Tanaka, *Mater. Trans.*, 2001, **42**, 2415–2421.
- V. Bérubé, G. Radtke, M. Dresselhaus, and G. Chen, *Int. J. Energy Res.*, 2007, **31**, 637–663.
- R. W. P. Wagemans, J. H. van Lenthe, P. E. de Jongh, A. J. van Dillen, and K. P. de Jong, *J. Am. Chem. Soc.*, 2005, **127**, 16675–16680.
- V. Bérubé, G. Chen, and M. S. Dresselhaus, *Int. J. Hydrog. Energy*, 2008, **33**, 4122–4131.
- J. Huot, D. B. Ravnsbæk, J. Zhang, F. Cuevas, M. Latroche, and T. R. Jensen, *Prog. Mater. Sci.*, 2013, **58**, 30–75.
- P. E. de Jongh and P. Adelhelm, *Chemsuschem*, 2010, **3**, 1332–1348.
- C. Zlotea and M. Latroche, *Colloids Surf. Physicochem. Eng. Asp.*, 2013, **439**, 117–130.
- R. Bogerd, P. Adelhelm, J. H. Meeldijk, K. P. de Jong, and P. E. de Jongh, *Nanotechnology*, 2009, **20**, 204019.
- P. E. de Jongh, R. W. P. Wagemans, T. M. Eggenhuisen, B. S. Dauvillier, P. B. Radstake, J. D. Meeldijk, J. W. Geus, and K. P. de Jong, *Chem. Mater.*, 2007, **19**, 6052–6057.
- Y. S. Au, M. Ponthieu, R. van Zwienen, C. Zlotea, F. Cuevas, K. de Jong, and P. de Jongh, *J. Mater. Chem. A*, 2013, **1**, 9983–9991.
- S. Bastide, C. Zlotea, M. Laurent, M. Latroche, and C. Cachet-Vivier, *J. Electroanal. Chem.*, 2013, **706**, 33–39.
- R. Campesi, F. Cuevas, R. Gadiou, E. Leroy, M. Hirscher, C. Vix-Guterl, and M. Latroche, *Carbon*, 2008, **46**, 206–214.
- J. P. A. Makongo, Y. Prots, U. Burkhardt, R. Niewa, C. Kudla, and G. Kreiner, *Philos. Mag.*, 2006, **86**, 427–433.
- S. Brunauer, P. H. Emmet, and E. Teller, *J. Am. Chem. Soc.*, 1938, **60**, 309–319.
- A. Michalowicz, J. Moscovici, D. Muller-Bouvet, and Provost, *J. Phys. Conf. Ser.*, 2009, **190**, 012034.
- A. L. Ankudinov, J. J. Rehr, and S. D. Conradson, *Phys. Rev. B*, 1998, **58**, 7565–7576.
- A. L. Ankudinov, C. E. Bouldin, J. J. Rehr, J. Sims, and H. Hung, *Phys. Rev. B*, 2002, **65**, 104107.
- P. I. Krypakevych and E. I. Gladyshevskii, *Sov. Phys.-Crystallogr.*, 1960, **5**, 552–554.
- IXS Standards and Criteria Committee, *Error Reporting Recommendations: A Report of the Standards and Criteria Committee*, International XAFS Society, 2000.
- J. Moscovici, A. Rougier, S. Laruelle, and A. Michalowicz, *J. Chem. Phys.*, 2006, **125**, 124505–124505–8.
- L. Sciortino, F. Giannici, A. Martorana, A. M. Ruggirello, V. T. Liveri, G. Portale, M. P. Casaletto, and A. Longo, *J. Phys. Chem. C*, 2011, **115**, 6360–6366.
- Y. Lei, J. Jelic, L. C. Nitsche, R. Meyer, and J. Miller, *Top. Catal.*, 2011, **54**, 334–348.
- L. Pasquini, F. Boscherini, E. Callini, C. Maurizio, L. Pasquali, M. Montecchi, and E. Bonetti, *Phys. Rev. B*, 2011, **83**, 184111.
- J. Harris, W. Curtin, and M. Tenhover, *Phys. Rev. B*, 1987, **36**, 5784–5797.
- R. Kirchheim, F. Sommer, and G. Schluckebier, *Acta Metall.*, 1982, **30**, 1059–1068.
- C. Rongeat, I. Llamas-Jansa, S. Doppiu, S. Deledda, A. Borgschulte, L. Schultz, and O. Gutfleisch, *J. Phys. Chem. B*, 2007, **111**, 13301–13306.
- S. A. Shevlin and Z. X. Guo, *J. Phys. Chem. C*, 2013, **117**, 10883–10891.
- Z. Zhao-Karger, J. Hu, A. Roth, D. Wang, C. Kübel, W. Lohstroh, and M. Fichtner, *Chem. Commun.*, 2010, **46**, 8353–8355.
- J. P. A. Makongo, Y. Prots, R. Niewa, U. Burkhardt, and G. Kreiner, *Z. Krist.-New Cryst. Struct.*, 2005, **220**, 291–292.
- J. P. A. Makongo, C. Kudla, Y. Prots, R. Niewa, U. Burkhardt, and G. Kreiner, *Z. Krist.-New Cryst. Struct.*, 2005, **220**, 289–290.
- M. A. Lillo-Rodenas, K. F. Aguey-Zinsou, D. Cazorla-Amoros, A. Linares-Solano, and Z. X. Guo, *J. Phys. Chem. C*, 2008, **112**, 5984–5992.
- F. Leardini, J. R. Ares, J. Bodega, J. F. Fernandez, I. J. Ferrer, and C. Sanchez, *Phys. Chem. Chem. Phys.*, 2010, **12**, 572–577.